Energy Reports 9 (2023) 4830–4843

Contents lists available at ScienceDirect

Energy Reports

journal homepage: www.elsevier.com/locate/egyr

Research paper

Effect of blade aspect ratio on the performance tradeoff between figure of merit and bending-torsion dynamics of wind turbines with synthetic jets

Victor Maldonado *, Nicolas Peralta, Wolduamlak Ayele, Dioser Santos, Guilherme Dufflis

Department of Mechanical Engineering, 2500 Broadway, Lubbock, TX, USA

ARTICLE INFO

Article history:
Received 8 July 2022
Received in revised form 6 March 2023
Accepted 4 April 2023
Available online xxxx

Keywords:
Rotor blade
Aerodynamics
Structural dynamics
Active flow control

ABSTRACT

In this experimental study, two three-bladed rotors with a blade aspect ratio of 7.79 and 9.74 representing a 25% increase were tested. Each blade contains an S809 airfoil with zero pre-built twist and 20 high-performance synthetic jet actuators distributed along the span. The rotor was tested at four rotor speeds, Ω of 250, 500, 750, and 1,000 revolutions per minute (RPM) and three collective blade pitch angles, θ_c of 2, 5, and 8 degrees. Rotor thrust was measured using a high-capacity load cell, and blade bending and torsion was measured at four equally spaced radial locations on the blade defined by $r/R = 0.24$, 0.48, 0.72, and 0.96 using four onboard inertial measurement units. The spanwise flow over the suction surface of the blade was measured using laser Doppler velocimetry (LDV) techniques. The local Reynolds number produced with the test rotor speeds at the measurement locations ranges from $8.31 \times 10^4 \leq Re_\infty \leq 9.49 \times 10^5$. It was found that rotor aerodynamic efficiency as quantified by the figure of merit is directly linked to blade aspect ratio and the magnitude of spanwise flow over the blade. The rotor with a higher blade aspect ratio produces less overall spanwise flow and is more aerodynamically efficient, however the blade also generates larger mean and fluctuating bending and torsion displacements, which are undesirable for aeroelastic stability. The use of synthetic jets on the blade mitigates the root mean square of the bending and pitch displacements above $\Omega = 250$ RPM and $\theta_c = 2°$. It was found that at $\Omega = 1{,}000$ RPM, the blade structures undergo a second mode bending response indicating a condition of structural instability due to higher aerodynamic loading. At this rotor speed, flow control on the outboard of the blade reduces unsteady bending as quantified by a_{rms} up to a maximum of 36.5%, and unsteady torsion, θ_{rms} up to 22.9% compared to the baseline for the rotor with an aspect ratio of 9.74.

1. Introduction

Wind turbine blades are semi-elastic structures and function in highly unsteady flow conditions, where the blades respond with multiple structural modes consisting of bending and torsion. Many types of passive and active blade-mounted flaps and fluidic actuators have been studied to control aerodynamic loads and vibration (Akhter and Omar, 2021). This is especially important as rotor blade span and aspect ratio become larger to improve the power capacity of the turbine. Trailing edge microtabs have been used extensively on fixed and rotating blades, showing the ability to increase or decrease the lift coefficient by up to 37% and 40% respectively at nominal operating conditions (Johnson et al., 2010). Deformable or semi-flexible flaps alter the nature of flow-blade interactions, leading to enhanced damping of the fluid–structure and an increase in attenuated fatigue loads on the rotor and transmission components (Zhang et al., 2015). When attempting to use flow control devices for aeroelastic control, it must be understood how aerodynamic and external loads are correlated to the blade's structural modes and vibration (Tibaldi et al., 2016), where the higher-order mode shapes are coupled between blade bending and twist (Acar and Feeny, 2018; Kallesoe, 2011). Various numerical approaches towards computing the aeroelastic response of blades using non-linear beam theory have been implemented (Gebhardt and Roccia, 2014; Ng et al., 2016), however experimental approaches to determine the structural dynamics of blades while in operation are lacking. This motivates the current investigation, where two wind turbine blades with 20 spanwise synthetic jet actuators and four accelerometers were tested as part of two three-bladed rotor configurations.

The two rotors contain blades with an S809 airfoil and an aspect ratio of 7.79 and 9.74, representing a difference of 25% between both blades. The parameter of aspect ratio, *AR* defined

* Correspondence to: Texas Tech University, USA.
E-mail address: victor.maldonado@ttu.edu (V. Maldonado).

https://doi.org/10.1016/j.egyr.2023.04.017

here as the blade span squared divided by planform blade area, b^2/S is studied in order to evaluate its impact on aerodynamic efficiency and aeroelastic stability. The blade aspect ratio of the first rotor ($AR = 7.79$) is a consequence of the design requirement of the blades to house 20 spanwise distributed piezo disk actuators for the synthetic jets. The increase of 25% in the aspect ratio for the second rotor is based on the belief that it is sufficiently higher than the first rotor to capture measurable differences in the flow and structural behavior, such at the amount of spanwise and chordwise flow, which will manifest itself in the aerodynamic coefficients and blade displacements. Keeping other blade design parameters the same, it is hypothesized that lower aspect ratios provide more aeroelastic stability by preventing excessive blade bending and torsional displacements, however aerodynamic lift and turbine power coefficient is compromised due to a lower blade section lift-curve-slope and lift-to-drag ratio (Kiefer et al., 2016).

The synthetic jet has emerged as an effective fluidic actuator capable of modifying the near-wall momentum and pressure distribution around an airfoil (Amitay et al., 2001) and virtually aeroshaping the airfoil by forming large mean recirculation zones (Mittal and Rampunggoon, 2002). This influences the aerodynamic forces and allows synthetic jets to be used for load control in unsteady flow conditions. Arrays of synthetic jets have been used on a finite span wind turbine blade with an S809 airfoil undergoing dynamic pitching, and as a consequence dynamic stall at a Reynolds number of 2.2×10^5 (Taylor and Amitay, 2015; Taylor et al., 2015). The aerodynamic coefficients and size of the hysteresis loop were modified to improve the post-stall behavior of the blade. A later study by the same research group performed dynamic stall experiments on a wind turbine blade model with an S817 airfoil at a Reynolds number of 3.75×10^5 and synthetic jet momentum coefficient of 0.012 (Rice et al., 2019). In addition, the synthetic jets were angled at 45 degrees to the surface of the airfoil which is uncommon in earlier literature. This is expected to provide more streamwise momentum closer to the wall. It was shown that the lift and pitching moment hysteresis was reduced depending on the reduced pitch frequency and amplitude. Synthetic jets have also been applied on vertical axis wind and water turbine models. Dynamic stall performance by improving suction pressure and thrust was reported for an experimental wind turbine blade with a NACA 0021 airfoil at $Re_c = 1.25 \times 10^5$ and low blade speed ratios between one and three (Yen and Ahmed, 2013). Results of a numerical study on a vertical axis water turbine using a time-accurate Reynolds-averaged Navier–Stokes (RANS) model increased the net torque and power output of the turbine, where the increment in net power was higher than the power consumed by the synthetic jets (Velasco et al., 2017).

Rotor blade rotation adds a significant degree of complexity to the flow introduced via inflow velocity as well as Coriolis and centrifugal forces. The aerodynamic performance of a low Reynolds number rotor ($\mathrm{Re} \approx 0.7–3.5 \times 10^5$) based on a NACA 0021 airfoil at speeds of 180 RPM and 240 RPM in hover and simulated forward flight at three freestream velocities; 10 m/s, 15 m/s, and 20 m/s was measured experimentally (Ma et al., 2020). It was demonstrated that synthetic jets increase the near-wall flow velocity, which reduces the pressure distribution over the upper surface of the blade and leads to delaying stall and producing higher lift coefficients. Flow measurements on rotating blades have also been acquired using laser Doppler velocimetry (LDV) inside the boundary layer (Maeda et al., 2014), and stereoscopic particle image velocimetry (SPIV) on the outer flow of a propeller blade (Ragni et al., 2011). The author's group has performed a series of rotor experiments with synthetic jet actuators adapted from fixed blade models (Maldonado et al., 2010b,a) to measure the flow with LDV techniques, and quantified the aerodynamic and aeroelastic performance of the rotor at transitional and turbulent flow regimes. A three-bladed wind turbine rotor based on an S809 airfoil with zero twist was tested at speeds of up to 1250 RPM, producing blade tip Reynolds number of approximately 10^6 based on local chord and freestream velocity. The main result is that synthetic jets reduce the net power input to drive the rotor by up to 10.6% at a rotor speed of 500 RPM and blade pitch angle of 3 degrees by improving the blade's overall lift-to-drag ratio (Maldonado and Gupta, 2019). This improves the power coefficient and power generated by the rotor.

A subsequent study with a three-bladed propulsive rotor with a NACA 0012 airfoil and zero twist was activated with synthetic jets using two different control schemes: non-constant synthetic jet momentum coefficient, C_μ (or constant velocity of 66.3 m/s for all synthetic jets) and constant C_μ per blade section by varying the jet velocity proportional to the local freestream velocity, which is approximately equal to the product of rotor speed and local radius, $U_\infty \approx \Omega r$ (Maldonado et al., 2021b). The findings show that for low rotor speeds below 500 RPM, constant C_μ control is preferred to reduce the synthetic jet momentum and blowing ratio (defined as the ratio of jet to freestream velocity) in the blade root region in order to avoid increasing the streamwise velocity deficit. It was also demonstrated that synthetic jet actuation is more effective relative to energy input in the blade tip region, where the rotor figure of merit was increased by up to 12.7% by reducing the velocity deficit and delaying flow separation in the blade tip region. A third study using the same experimental setup with the NACA 0012 rotor was performed to measure blade structural vibration, including mean and fluctuations of bending and torsion deflections, using three electronic accelerometers mounted inside the blade at three equidistant points along the span (Maldonado et al., 2021a). There is a non-linear relationship between rotor thrust and torque to blade bending (in the first flap mode) as well as torsion. The power spectral densities (PSD) exhibit a reduction in the power content of structural vibration at moderate to high rotor speeds and blade pitch angles by mitigating the fluctuations or root mean square component of the vibration. This is accomplished by injecting near-wall momentum with synthetic jets and minimizing unsteady flow recirculation which excites the blade at its natural frequency.

1.1. Research objectives

The main objective of this investigation is to experimentally investigate the effect of blade aspect ratio on the figure of merit and bending-torsion dynamics when synthetic jets are activated in the inboard or outboard region of the blade. The goal is to control and improve the aerodynamic performance of the blade while simultaneously control and avoid excessive blade bending and torsional displacements. The rotor thrust was measured using a high-capacity load cell, while blade bending and torsion were measured using four electronic accelerometers equally spaced inside the blade. Blade structural response in the first and second flap modes was computed using the mean and unsteady root mean square (rms) component of vibration.

2. Experimental methodology

A rotor testing tower (Maldonado and Gupta, 2019) and two three-bladed rotors instrumented with 20 high-performance piezo-driven synthetic jet actuators on each blade and four SignalQuest SQ-RPS rugged package accelerometers equally spaced inside one blade. The rotors were tested in a high-bay test cell where the effect of the ceiling can be neglected. The dimensionless ground height normalized by rotor radius, z/R was = 2.57 and 2.82 for the two rotors with a radius of 1.32 m and

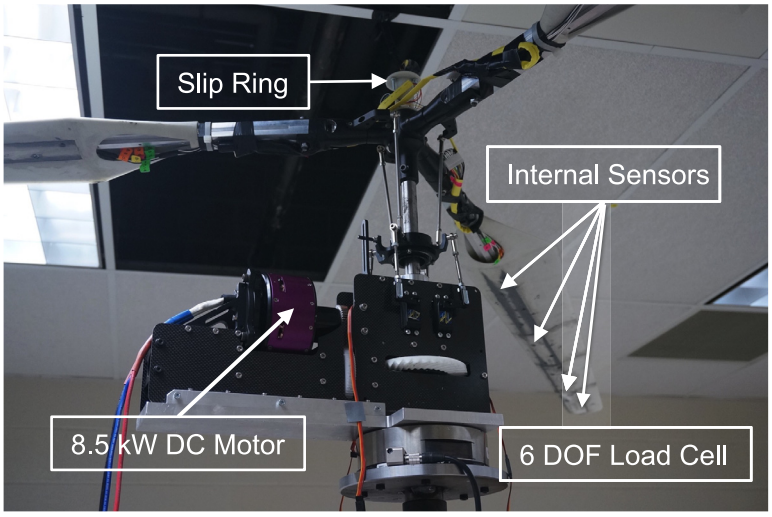

Fig. 1. Photograph of rotor assembly with main components (Maldonado et al., 2021a).

1.205 m respectively, and the expected increase in thrust from ground effect is approximately 1% (Cheeseman and Bennet, 1955). Each blade is rapid prototyped from nylon 12 glass-filled material in four modules which are screwed to an aluminum spar that provides bending and torsional stiffness. Both rotors contain an S809 airfoil with zero pitch distribution and a taper ratio, $\lambda = c_t/c_r$ of 0.5. All synthetic jet orifices are rectangular with a length, $l = 17.5$ mm and height, $h = 1.75$ mm (aspect ratio of 10) and are aligned parallel to the blade leading edge at a normalized chord location, $x/c = 0.40$ that coincides with the maximum thickness of the airfoil. The internal volume of each synthetic jet cavity is 194.3 mm^3, and determined from experiments to produce optimum resonance with 35 mm diameter piezo disks from Omega Piezo Technologies. Four high-torque servos control the collective pitch angle, θ_c of the blades, with an uncertainty of $\pm 0.2°$. A high-capacity ATI-IA model theta 6-component load cell is mounted to the rotor assembly to measure rotor thrust and torque. Load cell data was acquired with a National Instruments data acquisition board and a sampling rate of 1000 Hz for 20 s. The resolution in the rotor thrust and torque measurement is 0.25 N and 0.0125 N-m respectively. Lastly, A high-speed slip ring with 24 cable conductors is mounted to the rotor hub to route the necessary actuator and sensor cables between the rotor blades and the ground equipment. Fig. 1 is a photograph of the rotor assembly with main components during pre-testing of the rotor (Maldonado et al., 2021a). Table 1 describes the design and testing variables, normalized blade stiffnesses, and other key parameters for both rotors.

The synthetic jets were calibrated for maximum momentum transfer by driving the piezo disks with a sine wave amplified through a 3-channel piezo driver (Matsusada PZJ-J-0.1Px3) at a range of input frequencies from 1000 Hz to 2000 Hz. The jet velocity was measured at the center of the jet orifice exit plane using a Dantec Dynamics FiberFlow LDA system with a 60 mm optical probe. An optimum resonant frequency, f_{res} was found at 1570 Hz which produced a maximum average jet velocity, u_j of 67.4 m/s at a maximum of 50 V. The range of synthetic jet Reynolds number based on the minimum and maximum mean jet velocity and orifice height was calculated as $1638 \leq Re_j \leq 7832$. The jet momentum coefficient is a critical parameter that defines the momentum of the jet relative to the momentum of the flow over the blade defined as follows,

$$C_\mu = \frac{nI_j}{1/2\rho(\Omega r)^2 A_b} \tag{1}$$

Table 1
Rotor parameters and normalized stiffnesses.

Parameter	Symbol	Rotor 1 (R1)	Rotor 2 (R2)
Number of blades	n_b	3	3
Number of synthetic jets per blade	n_j	20	20
Airfoil	N/A	S809	S809
Airfoil thickness	t	0.21c	0.21c
Rotor radius	R	1.205 m	1.32 m
Blade span	b	1.06 m	1.18 m
Aspect ratio	AR	7.79	9.74
Taper ratio	λ	0.5	0.5
Blade mass	m_b	1.34 kg	1.57 kg
Rotational speed	Ω	250, 500, 750, 1000 RPM	Same
Blade collective pitch	θ_c	2°, 5°, 8°	2°, 5°, 8°
Young's modulus	E	3.58 GPa	3.58 GPa
Shear modulus	G	5.43 GPa	5.43 GPa
Lock number	$\frac{\rho C_{l_\alpha} cR^4}{I_b}$	5.47	7.18
Flap bending stiffness	$\frac{EI_\eta}{m_0\Omega^2R^4}$	[2.40, 38.36]	[1.83, 29.21]
Lead–lag bending stiffness	$\frac{EI_\xi}{m_0\Omega^2R^4}$	[44.12, 705.23]	[33.64, 537.01]
Torsional stiffness	$\frac{GJ}{m_0\Omega^2R^4}$	[7.27, 116.38]	[5.54, 88.61]

where Ωr is the product of rotor speed and local blade radius, which is approximately equal to the freestream velocity, U_∞ and varies linearly along blade span for a stationary rotor. The blade area, A_b, air density, ρ, and n is the number of synthetic jets on each blade which ranges from 4 to 20 depending on the modules activated. Finally, I_j is the time-average jet momentum during the piezo outstroke which solely imparts momentum to the external flow,

$$I_j = \frac{1}{2}\rho A_{sj} \int_o^\tau u_j^2(t)\, dt \tag{2}$$

where τ is the dimensionless synthetic jet duty cycle during the outstroke of the actuation cycle, A_{sj} is the area of the synthetic jet orifice (30.63 mm^2), and $u_j(t)$ is the centerline velocity at the orifice. The momentum coefficient for a certain blade module is calculated by considering the number of synthetic jets in the module, the mean jet velocity, the freestream velocity computed at the center of the module, and the module planform area. The range of synthetic jet momentum coefficients produced for the rotor experiments is $0.00289 \leq C_\mu \leq 0.132$ for rotor 1, and $0.00178 \leq C_\mu \leq 0.114$ for rotor 2. The lowest value in the range

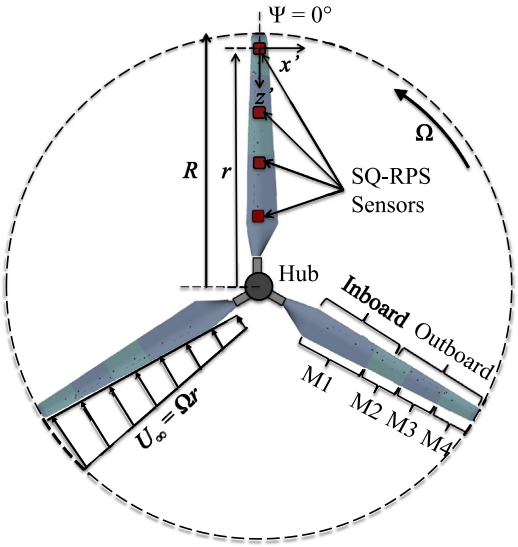

Fig. 2. Schematic of a rotor showing: SQ-RPS sensors on one blade at four radial locations, blade modules M1–M4 with inboard and outboard regions, and an approximate linear freestream velocity distribution.

for both rotors represents activating the outboard synthetic jets at a rotor speed of 1000 RPM, while the highest value represents activating the inboard synthetic jets at 250 RPM. Note that all synthetic jets on the blades were activated with a mean jet velocity of 67.4 m/s, producing relatively large momentum coefficients in the inboard region of the blade at low rotor speeds.

The rotor blade is considered a semi-rigid structure which undergoes vibration due to the unsteady fluids environment and aerodynamic forces. The dynamics of the blade are a result of primarily non-linear inertial couplings between blade flap, lag, and torsion at different rotor speeds and collective pitch angles. This results in large rigid-body displacements with some deformation along rotor radius. One of the three rotor blades on both rotors was instrumented with four SignalQuest SQ-RPS rugged package sensors at four equally spaced radial locations, $r/R =$ 0.24, 0.48, 0.72, and 0.96 inside the blade beneath a synthetic jet. The SQ-RPS sensors are capable of measuring local tri-axis linear acceleration (x, y, z) and angular position given by pitch, roll, and yaw angles. A digital filter minimizes noise from external sources, and each sensor achieves a baseline resolution of ± 0.005 g and $\pm 0.1°$ on each axis. The output from the sensors was tested with all piezoelectric disks on the blade powered on, which reduced the signal accuracy to approximately ± 0.012 g and $\pm 0.2°$. Sensor data was acquired at a sampling rate of 1000 Hz for 20 s at a steady-state rotor speed and collective blade pitch angle. Synthetic jets were activated 5 s prior to sensor data acquisition in order to improve steady state blade dynamics. During every test case, blade azimuthal position is tracked using a Hall-effect sensor mounted near the rotor shaft and is referenced from the angle, $\Psi = 0°$. The synthetic jets were activated in various groups: (i) blade modules 1–4 where all 20 synthetic jets are activated, (ii) modules 3–4 with 8 jets, (ii) inboard region of the blade with 10 jets, and (iv) outboard region of the blade with 10 jets. The inboard region is the area of the blade from a rotor radius, $r/R =$ 0.20 to 0.60, while the outboard region extends from $r/R = 0.60$ to 1.0. A schematic of the rotor depicting the SQ-RPS sensors on one blade are illustrated on Fig. 2.

The dynamics of the rotor blade are described with Fig. 3(a). Each sensor contains its own cartesian coordinate system, where relevant blade motion is measured along four degrees-of-freedom: blade bending along the $y'-z'$ plane, blade roll angle, ϕ, and torsional motion about the blade pitch angle, θ. Each sensor is fixed rigidly to the bottom of the blade structure, and is located below a synthetic jet and centered at a chordwise position, x/c $= 0.40$ as depicted on Fig. 3(b). The four spanwise sensors and experimental analysis captures the first and second flap bending mode dynamics of the blade.

Table 2
Local flow Reynolds and Mach number for both rotors at the sensor locations.

Ω (RPM)	r/R	R1: Re_∞	R2: Re_∞
250	0.24	8.31×10^4	8.46×10^4
500	0.24	1.66×10^5	1.69×10^5
750	0.24	2.49×10^5	2.54×10^5
1000	0.24	3.32×10^5	3.39×10^5
250	0.48	1.48×10^5	1.52×10^5
500	0.48	2.96×10^5	3.05×10^5
750	0.48	4.44×10^5	4.57×10^5
1000	0.48	5.91×10^5	6.10×10^5
250	0.72	1.94×10^5	2.03×10^5
500	0.72	3.88×10^5	4.07×10^5
750	0.72	5.83×10^5	6.10×10^5
1000	0.72	7.77×10^5	8.13×10^5
250	0.96	2.22×10^5	2.37×10^5
500	0.96	4.44×10^5	4.74×10^5
750	0.96	6.66×10^5	7.11×10^5
1000	0.96	8.89×10^5	9.49×10^5

2.1. Experimental conditions

The rotors were tested at four rotor speeds, Ω of 250, 500, 750, and 1000 RPM and three collective blade pitch angles, θ_c of 2, 5, and 8 degrees. The collective pitch angles were selected for normal blade operation and to avoid significant flow separation which occurs in the stall region of the S809 airfoil. Thus, the collective pitch angle values are low to moderate and lie close together so that the effective angle of attack along the blade is within or near the linear lift-curve-slope of the airfoil. The exception is the flow over the blade tip region which operates in near-stall and mild stall conditions at a rotor speed of 750 RPM and above, and with a pitch angle of 6 degrees and above (Maldonado and Gupta, 2019). The pitch angles are calibrated with a digital protractor prior to operating the rotor, and the error is estimated as $\pm 0.2°$. The local flow Reynolds number at the location of the SQ-RPS sensors, r/R is calculated according to $Re = U_\infty c/\nu$, where c is the local airfoil chord and ν is the air kinematic viscosity. The Reynolds number for all rotor speeds at the sensor locations for both rotors are given on Table 2.

3. Results

3.1. Aerodynamic efficiency

The aerodynamic efficiency of the rotors with different blade aspect ratio is quantified with the figure of merit, *FM* and thrust coefficient, C_T. The distribution of aerodynamic lift, drag, and pitching moment per unit span strongly influence the structural response of the blade. The role of synthetic jets is to control the local external flow, and thereby the airfoil aerodynamic coefficients which vary as a function of span. The *FM* is defined as the ratio of the ideal to actual power required to generate a given thrust, T with a rotor disk area, A and air density, ρ,

$$FM = \frac{P_{ideal}}{P_{actual}} = \frac{\frac{T^{3/2}}{\sqrt{2\rho A}}}{P_{elec}} \tag{3}$$

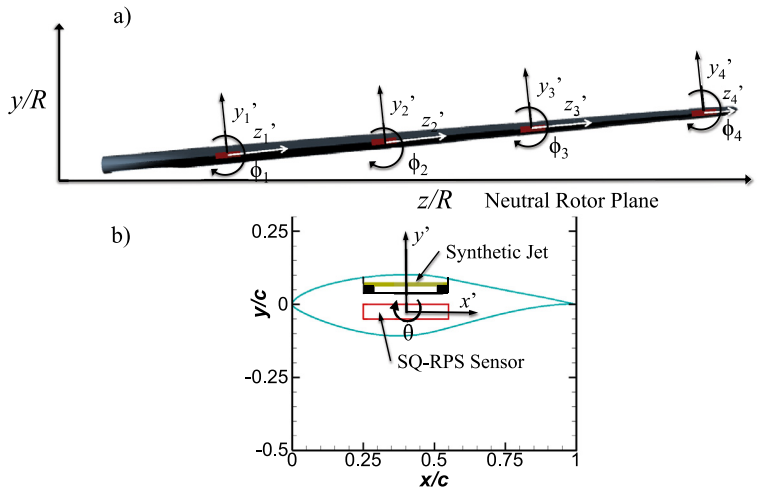

Fig. 3. Schematic of rotor blade: (a) Placement of SQ-RPS sensors with local coordinate systems and (b) S809 airfoil cross-section showing location of synthetic jet and sensor.

The C_T measures the rotor's ability to produce thrust relative to the rotor disk area and its blade tip speed (ΩR),

$$C_T = \frac{T}{\rho A(\Omega R)^2} \tag{4}$$

The *FM* is plotted as function of C_T for blade pitch angles of $\theta_c = 2°$, 5°, and 8° respectively in Fig. 4(a, b, and c). The main distinction between both rotors is that the higher blade aspect ratio of rotor 2 increases the figure of merit while decreasing the thrust coefficient. The flow over the rotor blades behave slightly differently and manifests itself by altering the aerodynamics of the rotor. The magnitude of spanwise flow, W/U_∞, which does not contribute to lift generation, for R2 is measured to be lower compared to R1. Based on the flow physics, when integrated along the entire blade surface, it is expected that the three-dimensional lift-curve-slope of R2 throughout the blade is higher, increasing the blade section lift coefficient, C_L at a given angle of attack and therefore producing more total blade lift and rotor thrust . Another consequence of higher blade aspect ratio is the reduction in induced drag coefficient, as defined for finite wings by the common expression, $C_{D_i} = kC_L^2$, where $k = \frac{1}{\pi AR e}$. The marginal increase in C_L^2 for R2 due to the flow behavior as explained earlier is overshadowed by the 25% reduction in k due to aspect ratio, which decreases the induced drag and overall drag coefficient, C_D for the R2 blades. The actual power in the *FM* calculation is thus also reduced, since the rotor power and torque can be shown to be directly related to blade drag.

As noted earlier, the thrust coefficient decreases for rotor blades with higher aspect ratio. The net increase in thrust of R2 is less than the increase in the quantity $A(\Omega R)^2$, which occurs from having a larger rotor radius. This is consistent with a lower disk loading, which reduces the power required to maintain a given rotor speed and indicates improved thrust efficiency. However, the blade structural response of R2 indicates that this efficiency comes at the expense of higher blade displacements, which in most cases is considered undesirable. The role of flow control relative to the baseline cases is to improve both the C_T and *FM* values. Moreover activating synthetic jets on blade modules M3-4 achieves better *FM* results and requires less piezo energy input compared to all modules (M1-4) for lower rotor speeds of Ω = 250 and 500 RPM. This demonstrates that synthetic jets near the root to middle region of the blade (M1-2) should not be used at low rotor speeds and blade pitch angles due to two reasons; the boundary layers are attached and stable in these conditions and jet activation will not generally reduce the velocity deficit in the near-wall flow to affect the blade sectional lift or drag coefficient. Second, if the blowing coefficient, C_b, defined as the ratio of jet velocity to local freestream velocity is sufficiently high ($C_b \gtrsim 3$), the streamwise flow going over the blade at the location of the jet will undergo a velocity deficit which decreases the resulting aerodynamic efficiency of the blade in this region (Maldonado et al., 2021b). Furthermore, at high rotor speeds of Ω = 750 and 1000 RPM, the case of M1-4 jet activation only marginally improves the C_T and *FM* performance of the rotors compared to the M3-4 case. The *FM* results also show that increasing collective pitch angle from $\theta_c = 2°$ to 8° places the rotor blade to operating with more optimum aerodynamic efficiency in terms of higher overall lift-to-drag ratio. It is important to note that since the rotor blades do not have pre-built twist distribution, the profile power of the blade increases as a function of span (Bagai, 2008). In addition, the rotor suffers from unsteady aerodynamic effects of dynamic stall in the blade tip region at high speeds, which limits the *FM* values that can be attained compared to a rotor blade with some form of twist.

3.2. Three-dimensionality of the flow

Rotor blades experience a high degree of flow 'three-dimensionality' and spanwise flow structures due to the rotating blade which generates Coriolis forces. It is hypothesized, however, that increasing the aspect ratio (*AR*) of a blade will reduce the spanwise flow component, W/U_∞ while increasing the chordwise flow component, U/U_∞ (which is desired on an airfoil to produce lift) in the middle region of the blade away from the blade root and tip. The rotor hub and strong blade tip vortex adds interference and induces additional spanwise flow that increases W/U_∞ in these two regions (Maldonado and Gupta, 2019). The figure of merit results presented earlier indicate that Rotor 2 with higher *AR* produces sightly more thrust for a given rotor power compared to Rotor 1, and is believed to be attributed to less overall flow three-dimensionality. In order to test this hypothesis, the flow over the suction surface of a blade on both rotors was measured at four dimensionless rotor stations, r/R = 0.24, 0.48, 0.72, and 0.96 using phase-locked LDV techniques, according to the methodology described in earlier studies by the author (Maldonado et al., 2021b,a). At each station, the magnitude of spanwise flow is plotted as a function of the dimensionless local blade chord for nine equally spaced chordwise positions, x/c = 0.1 to 0.9, where x/c = 0 represents the leading edge of the airfoil. Due to the boundary layer growth with chordwise

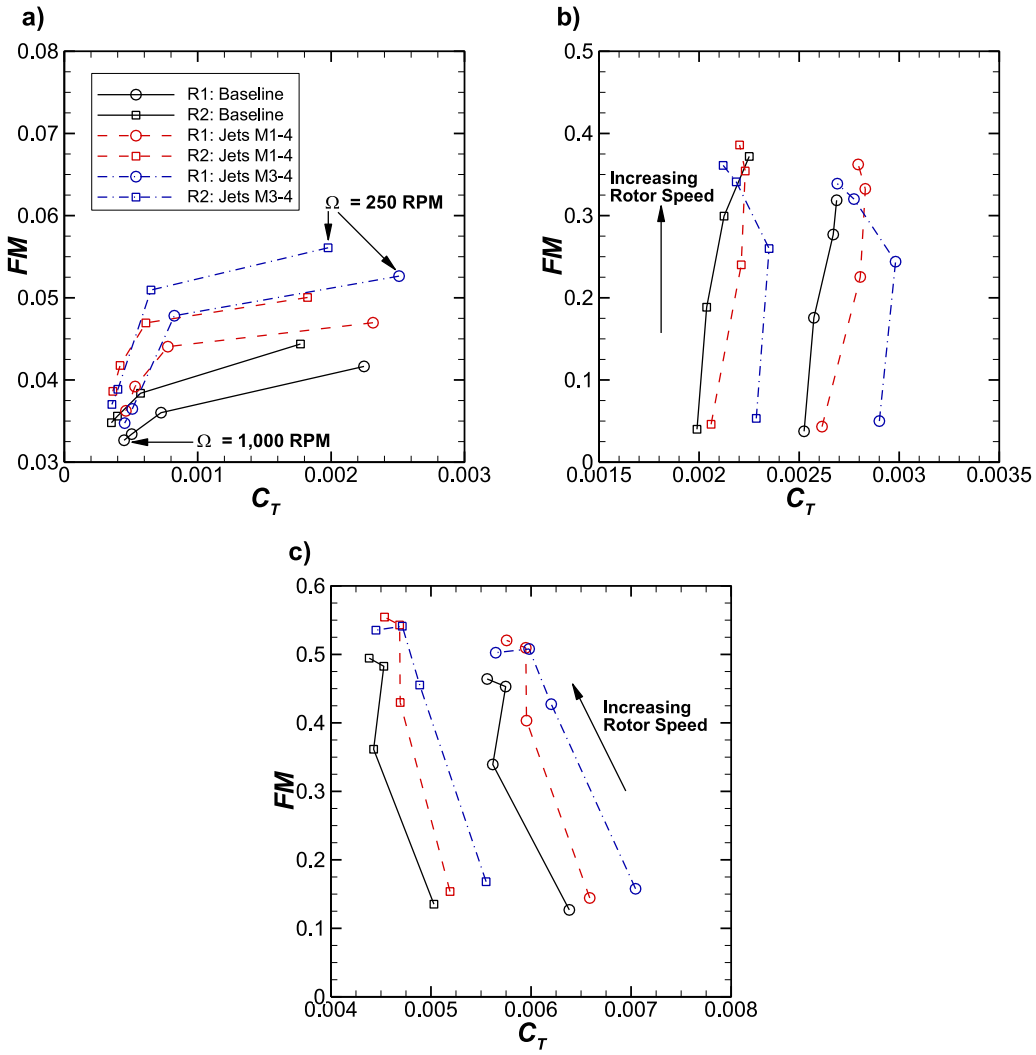

Fig. 4. Rotor figure of merit: (a) $\theta_c = 2°$, (b) $\theta_c = 5°$, and (c) $\theta_c = 8°$.

distance, the LDV measurement domain was traversed away from the blade surface (in the wall-normal direction, y') such that data at each position was acquired at approximately the boundary layer thickness, δ where $U = U_\infty \pm 3.6\%$. It was previously determined that synthetic jets do not have an appreciable effect on the spanwise flow (Maldonado and Gupta, 2019), therefore measurements with flow control are not presented.

Results at a rotor speed of $\Omega = 500$ RPM are presented on Fig. 5. The spanwise flow is lowest at $r/R = 0.48$ and increases in a complex nonlinear fashion with radial distance towards the blade root ($r/R = 0.24$) and becomes even more pronounced towards the outboard region of the blade at $r/R = 0.72$ and 0.96 due to the blade tip vortex interaction. Spanwise flow also generally increases, and the flow seems to 'meander' (based on the magnitude of W/U_∞) as it travels from the leading edge of the blade to the trailing edge. This flow phenomena becomes more severe when the rotor speed is increased further to $\Omega =$ 1000 RPM in Fig. 6. This may be due to transition and crossflow instabilities with higher Reynolds numbers. There is no apparent dependence of W/U_∞ with the blade pitch angle when the flow is attached, however spanwise flow marginally increases when the flow begins to separate for $\theta_c = 8°$ at $r/R = 0.72$ and 0.96.

When comparing the effect of aspect ratio on the three-dimensionality of the flow over the rotor blade, it can be observed that rotor 2 with higher *AR* contains between 8%–14% lower magnitude of W/U_∞ compared to rotor 1 in the middle region of the blade at $r/R = 0.48$. This benefit is reduced away from this region and becomes negligible at the root and tip region of the blade, as there is very little difference in the three-dimensionality of the flow. We can conclude that there is strong evidence to suggest that rotors with higher aspect ratio blades are more aerodynamically efficient from increased operating lift-to-drag, L/D ratios (as is the case with fixed wings) which is a result of maintaining quasi two-dimensional flow by reducing the spanwise flow component.

3.3. Rotor blade structural response

The effect of aspect ratio and synthetic jet actuation on the blade's bending and torsion dynamics was studied in order to determine satisfactory performance tradeoffs between the rotor figure of merit, which represents aerodynamic efficiency, and blade displacements. Flow control was activated in different regions of the blade defined as follows; on the inboard region ($0.20 \leq r/R \leq 0.60$) where the first 10 jets were activated, and on the outboard region ($0.60 \leq r/R \leq 1.0$) where the second set of 10 jets were activated, and are represented as FC-I and FC-O respectively. The blade's mean bending displacement at each sensor was computed along the y' and z' axes via double integration of the acceleration measurements according to $y' = 0.5 a_{y'} t^2$ and

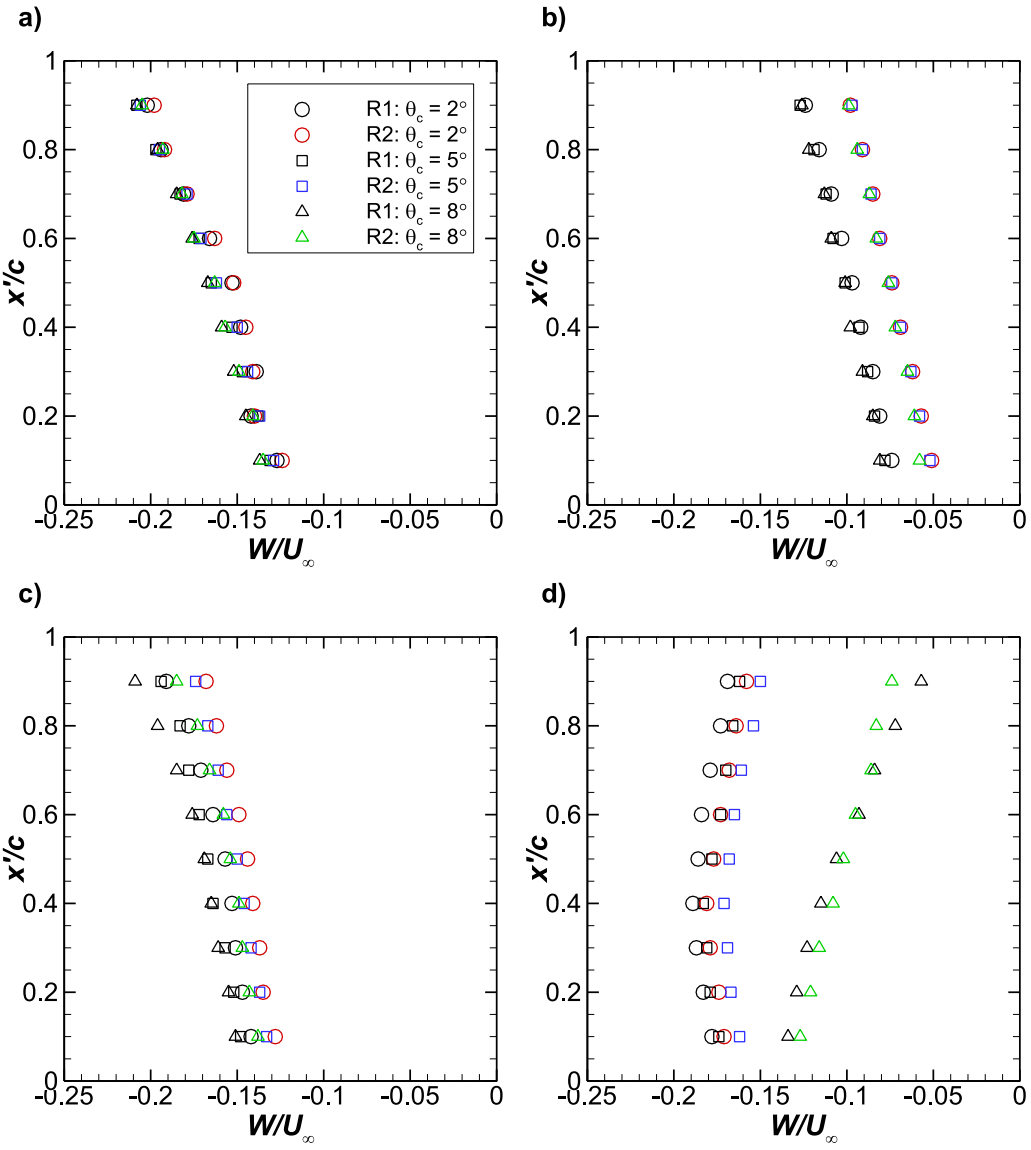

Fig. 5. Profiles of normalized spanwise velocity, W/U_∞ at $\Omega = 500$ RPM for rotor 1 (R1) and rotor 2 (R2): (a) $r/R = 0.24$, (b) $r/R = 0.48$, (c) $r/R = 0.72$, and (d) $r/R = 0.96$.

$z' = 0.5a_{z'}t^2$. In order to neglect the displacement error incurred from integration of acceleration, the sensor output was calibrated to position by factoring in the blade's bending and torsional moment of inertia. The y' and z' variables were transformed into the $y-z$ reference frame and normalized with each rotor's radius, R to obtain dimensionless variables, y/R and z/R. Mean blade bending for the baseline (BL) rotors R1 and R2 as well as with flow control are shown on Fig. 7 for rotor speeds of $\Omega = 250$ and 500 RPM and collective pitch angles, $\theta_c = 2°$, 5°, and 8°.

At lower rotor speeds of $\Omega = 250$ and 500 RPM, aerodynamic loading causes both blades to undergo relatively linear bending displacements (y/R) as a function of rotor radius. There is a subtle difference in displacement with flow control. For both rotors, activating jets in the outboard region of the blade produces slightly higher blade displacements throughout the blade compared to using jets in the inboard region. This is due to the higher bending moment produced by enhancing lift in the outboard of the blade which is further away from the rotor hub. Moreover at these lower rotor speeds, it was shown in a previous study that using synthetic jets closer to the blade root often produce elevated levels of synthetic jet momentum coefficient, C_μ and blowing ratio C_b, which increases the velocity deficit in the near-wall flow and reduces the blade's sectional lift coefficient (Maldonado et al., 2021b). There is significant increase in mean blade displacement at $\Omega = 750$ and 1000 RPM for all collective pitch angles. More importantly for the significance of this study, R1 with a lower aspect ratio slightly reduces bending displacements particularly in the outboard blade region compared to R2. This is due to the lower radius of R1 and its increased spanwise flow which reduces the airfoil's lift-curve-slope and ability to produce lift per unit span.

When the rotor speed is increased to $\Omega = 1000$ RPM represented by the plots of Fig. 8(d, e, f), the results indicate that both rotors undergo a shift from the first bending mode to the second mode.

There is a distinctive inflection point in the bending behavior as observed by a reduction in the slope between the relative position of the two outboard sensors at $z/R = 0.72$ and 0.96 compared to that of the two inboard sensors at $z/R = 0.24$ and 0.48. Furthermore, increasing the blade pitch to $\theta_c = 5°$ and 8° increases the severity of the modal response, as measured by a dramatic increase in the slope between the position of the

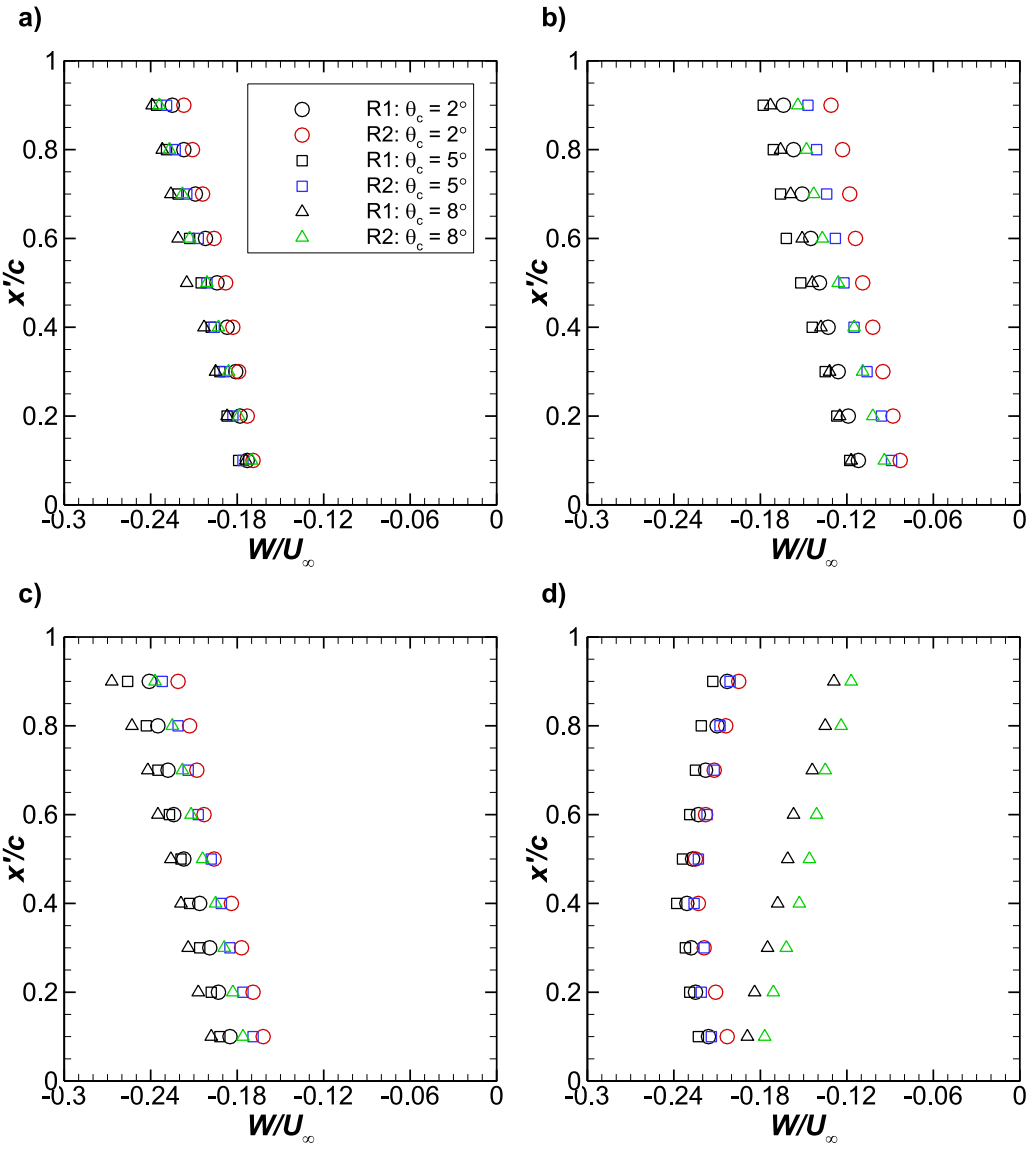

Fig. 6. Profiles of normalized spanwise velocity, W/U_∞ at $\Omega = 1000$ RPM for rotor 1 (R1) and rotor 2 (R2): (a) $r/R = 0.24$, (b) $r/R = 0.48$, (c) $r/R = 0.72$, and (d) $r/R = 0.96$.

inboard and onboard sensors. Rotor 1 thrust and flow measurements from a previous study reveal that at $\Omega = 1000$ RPM for moderate pitch angles, aerodynamic loading is significant and highly non-linear with flow separation initiating in the blade tip region (Maldonado and Gupta, 2019). The use of synthetic jets distributed along the blade span is to finely control, and in most cases, increase the magnitude of mean blade bending due to delaying flow separation and improving lift production (Maldonado et al., 2021b). Activating jets on the outboard region of the blade, as explained earlier, is more effective in contributing to blade bending.

Unsteady blade bending was measured by quantifying the root mean square (rms) of the acceleration, a_{rms} from each sensor on the rotor blade. The time histories of a_{rms} from each sensor were utilized to compute the mean power spectral density (PSD) of the blade for each operating condition. When plotted in the frequency domain, the peak of the PSD, and therefore the highest power content coincides at the natural frequency, ω_n of the blade. The natural frequencies in the first flap mode are directly dependent on rotor speed and are given on Table 3 for the baseline R1 and R2 case. Activating the synthetic jets reduces the amplitude of blade vibration and the magnitude of the PSD peak, however the natural frequencies remain the same within the bounds of the given uncertainty.

Table 3
First flap mode natural frequencies for the baseline R1 and R2 case.

Ω (RPM)	R1 ω_n (Hz)	R2 ω_n (Hz)
0	10.4 ± 0.1	9.5 ± 0.1
250	11.6 ± 0.3	10.5 ± 0.3
500	13.1 ± 0.6	11.7 ± 0.6
750	14.9 ± 1.0	13.3 ± 1.0
1000	17.7 ± 1.5	15.8 ± 1.5

The root mean square of blade bending acceleration is presented on Fig. 9 for rotor speeds of $\Omega = 250$ RPM and 500 RPM. The fluctuating component of acceleration displays an exponential relationship with rotor radius and generally increases in magnitude with collective pitch angle and rotor speed. Moreover, the a_{rms} of R1 is always higher than R2 due to its lower mass and blade span which is a result of the rotor's natural frequency, ω_n in the first flap mode as shown on Table 3. At a low rotor speed

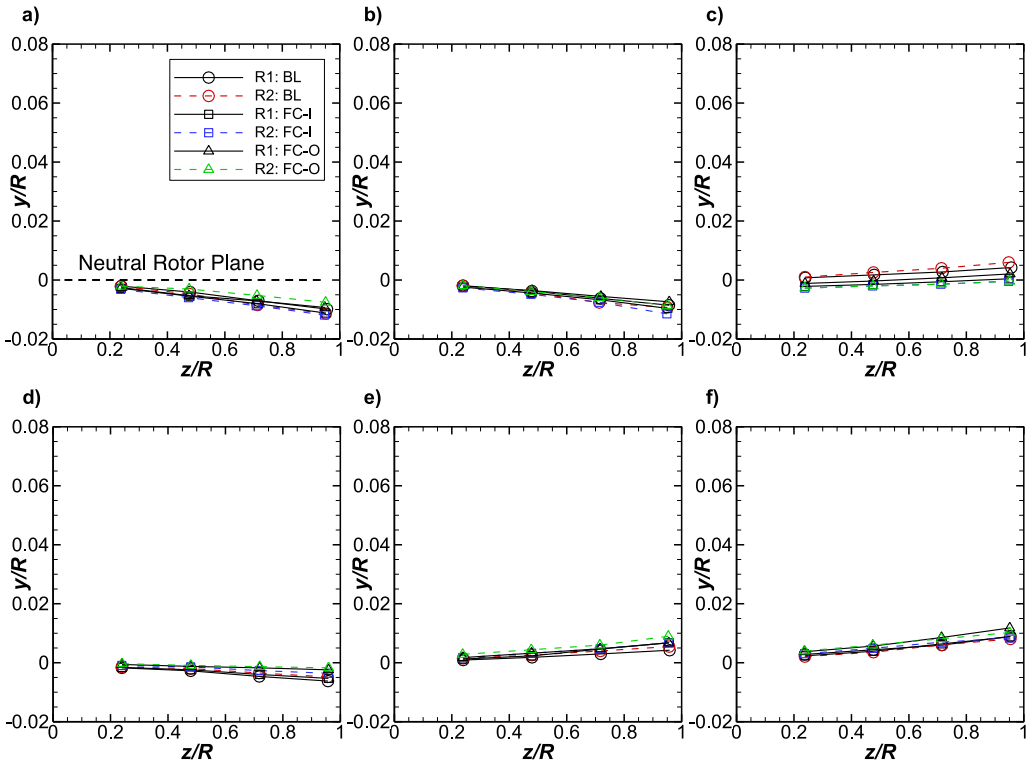

Fig. 7. Mean blade bending for the baseline and flow control cases at a rotor speed of $\Omega = 250$ RPM: (a) $\theta_c = 2°$, (b) $\theta_c = 5°$, (c) $\theta_c = 8°$ and $\Omega = 500$ RPM: (d) $\theta_c = 2°$, (e) $\theta_c = 5°$, (f) $\theta_c = 8°$.

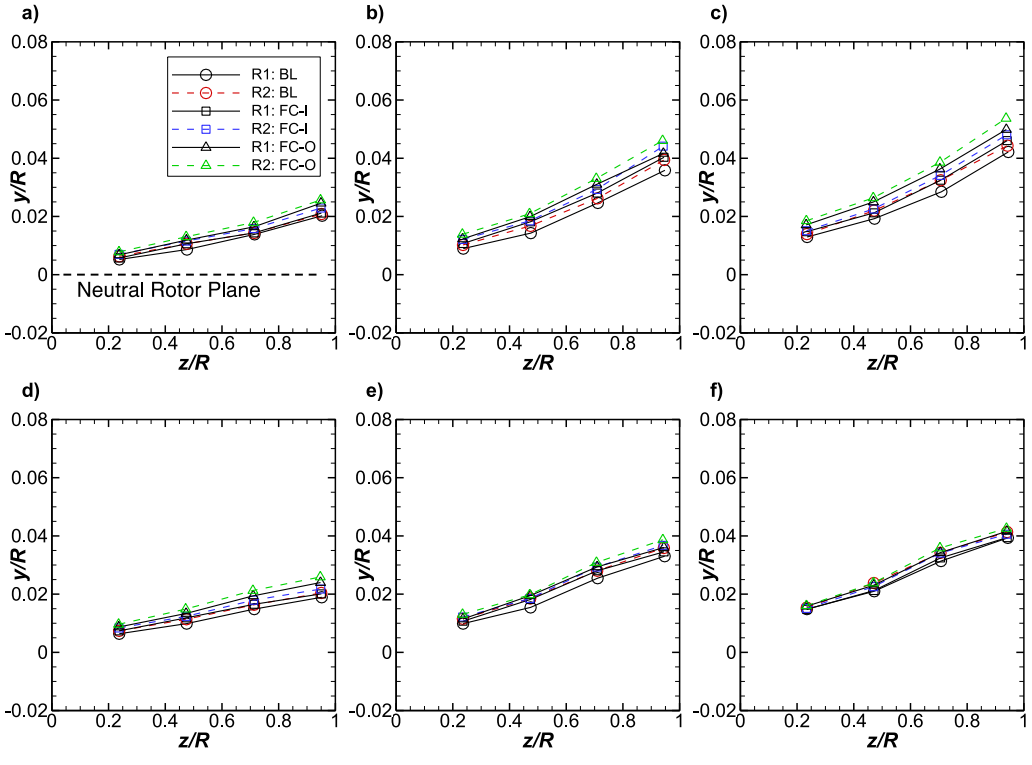

Fig. 8. Mean blade bending for R1 and R2 at a rotor speed of $\Omega = 750$ RPM: (a) $\theta_c = 2°$, (b) $\theta_c = 5°$, (c) $\theta_c = 8°$ and $\Omega = 1000$ RPM: (d) $\theta_c = 2°$, (e) $\theta_c = 5°$, (f) $\theta_c = 8°$.

of $\Omega = 250$ RPM, using flow control on the inboard region of the blade increases a_{rms} and makes unsteady vibration worse.

In this case, the momentum flux provided by synthetic jets can induce a local velocity deficit or flow separation if the blowing ratio is excessive in the inboard region, or the effect of synthetic jets is minimally favorable because they are not being used to delay flow separation, as is the case in the outboard blade region. A calculation of the blowing ratio for the jets on R1 located at

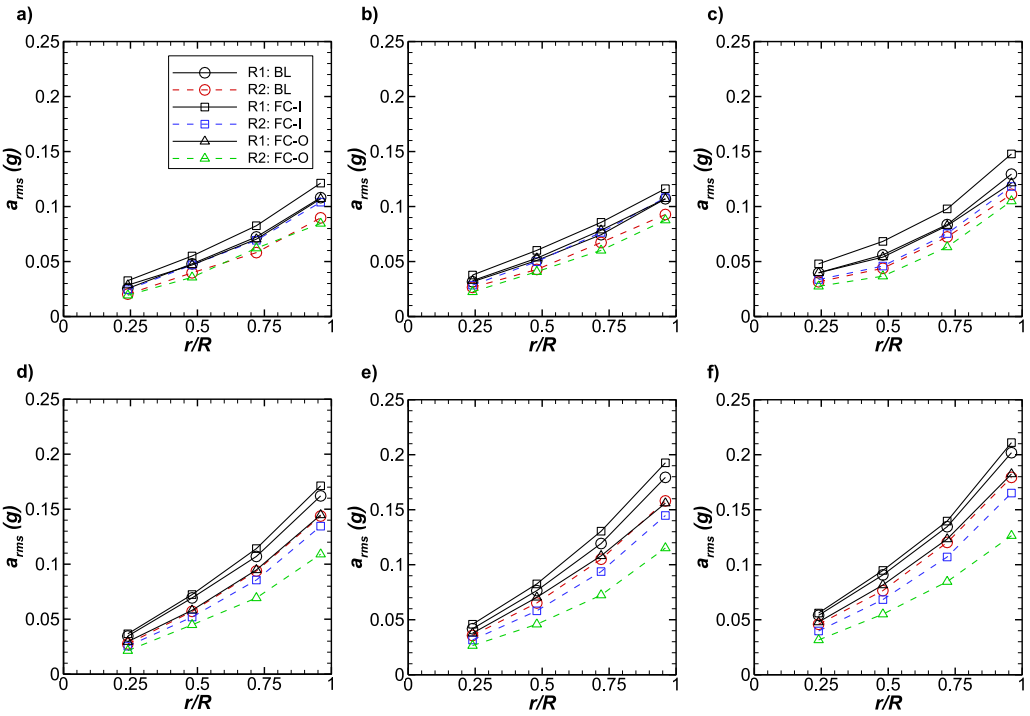

Fig. 9. Root mean square of the blade bending acceleration for R1 and R2 at a rotor speed of $\Omega = 250$ RPM: (a) $\theta_c = 2°$, (b) $\theta_c = 5°$, (c) $\theta_c = 8°$ and $\Omega = 500$ RPM: (d) $\theta_c = 2°$, (e) $\theta_c = 5°$, (f) $\theta_c = 8°$.

$r/R = 0.40$ and 0.80 which represent the middle of the inboard and outboard regions respectively, reveal that $C_b = 5.93$ and 2.54. The C_b value of 5.93 is above the threshold of approximately 3.0 which results in adverse effects that reduce the airfoil section's lift coefficient and thus figure of merit, and contribute to unsteady vibration as observed in the results. However, the use of synthetic jets on the outboard region of the blade, especially at $\Omega = 500$ RPM and $\theta_c = 8°$, significantly reduces unsteady vibration at every sensor along the blade radius. For R1 the percentage reduction in the baseline a_{rms} from the sensors at the blade tip at $r/R = 0.96$ to the root at r/R at 0.24 is in the range of 9.6% $\leq a_{rms} \leq$ 11.3%. The reduction in baseline a_{rms} for R2 is more pronounced and is in the range of 28.2% $\leq a_{rms} \leq$ 31.1% for these same conditions. This signifies that synthetic jets are more effective in further mitigating a_{rms} if the blade is already operating with a lower level of unsteady blade bending (see Fig. 10).

At a rotor speed of $\Omega = 750$ RPM, the behavior of a_{rms} as a function of rotor radius shows a mild logarithmic dependence for some cases. This departure from an exponential behavior may be due to the abrupt effect of boundary layer transition and a combination of laminar and turbulent flow appearing on the blade, where the local Reynolds number for both rotors ranges from $2.48 \times 10^5 \leq Re_\infty \leq 6.86 \times 10^5$ respectively from $0.24 \leq r/R \leq 0.96$. It is hypothesized that transition and higher turbulence intensity leads to a more drastic rise in unsteady vibration, which can be observed when the rotor speed is increased to $\Omega = 1000$ RPM. Under these conditions, turbulent flow dominates most of the rotor and the boundary layer begins to separate in the blade tip region (Maldonado et al., 2021b). The magnitude of unsteady vibration at $r/R = 0.96$ reaches a maximum of $a_{rms} = 0.80g$ for R1 baseline at $\theta_c = 8°$. The application of flow control on the outboard blade region is able to reduce unsteady vibration to $a_{rms} = 0.51g$, which represents a significant 36.5% reduction.

3.4. Blade torsion dynamics

The torsion dynamics of the blades were also quantified in terms of the mean and root mean square of the pitch angle at every sensor location. The blade mean pitch angle, θ increases fairly linearly with span near the root from, $r/R = 0.24$ to the tip, $r/R = 0.96$ at low rotor speeds of $\Omega = 250$ RPM and 500 RPM, as presented in Fig. 11. The S809 airfoil generates a positive nose pitch-up moment coefficient about the location of the sensor at $x/c = 0.4$, or $C_{m_{0.4}}$ for positive angles of attack. The torsional motion of the blade is then manifested from the pitching moment, which is an integration of the unsteady aerodynamic pressure and shear stress forces along the blade chord and span, resulting in a surface integral. Flow control is observed to increase the blade pitch for both blades, which is explained by the fact that synthetic jets increase the mean lift of the blade and pitching moment for most conditions. This behavior acts to apply a twisting moment to the blade during operation, therefore increasing the local pitch angle to a higher angle from its initial collective pitch angle set at the hub close to $r/R = 0$.

As the rotor speed is increased to 750 RPM and 1000 RPM in Fig. 12, aerodynamic loading and blade torsion becomes nonlinear, where the torsion gradient, $^{d\theta}/_{dr/R}$ is considerably higher in the outboard blade region between $r/R = 0.72$ to 0.96 compared to the inboard region between $r/R = 0.24$ to 0.48. However, this behavior is an exception of blade torsion for two specific cases; $\Omega = 1000$ RPM with $\theta_c = 5°$ and 8°, where the torsion gradient actually decreases slightly on the outboard blade region. This is attributed to the onset of flow separation and thus a reduction in the pitching moment produced in the blade tip region at moderate and high rotor speed and collective pitch angles. The magnitude of total torsional twist from $r/R = 0.24$ to 0.96 was largest for R2 which has the higher aspect ratio, and suggests that a longer blade is more susceptible to torsional structural instabilities despite being more efficient aerodynamically. As an example to highlight this phenomenon, the blade response at $\Omega = 750$ RPM with $\theta_c = 8°$ (Fig. 12c) shows that for R1 and R2 baseline, the total twist, θ_T is 1.8° and 2.2° respectively. Applying flow control on the outboard blade for both rotors increases θ_T to 2.9° and 3.2°, and is a significant additional torsional displacement.

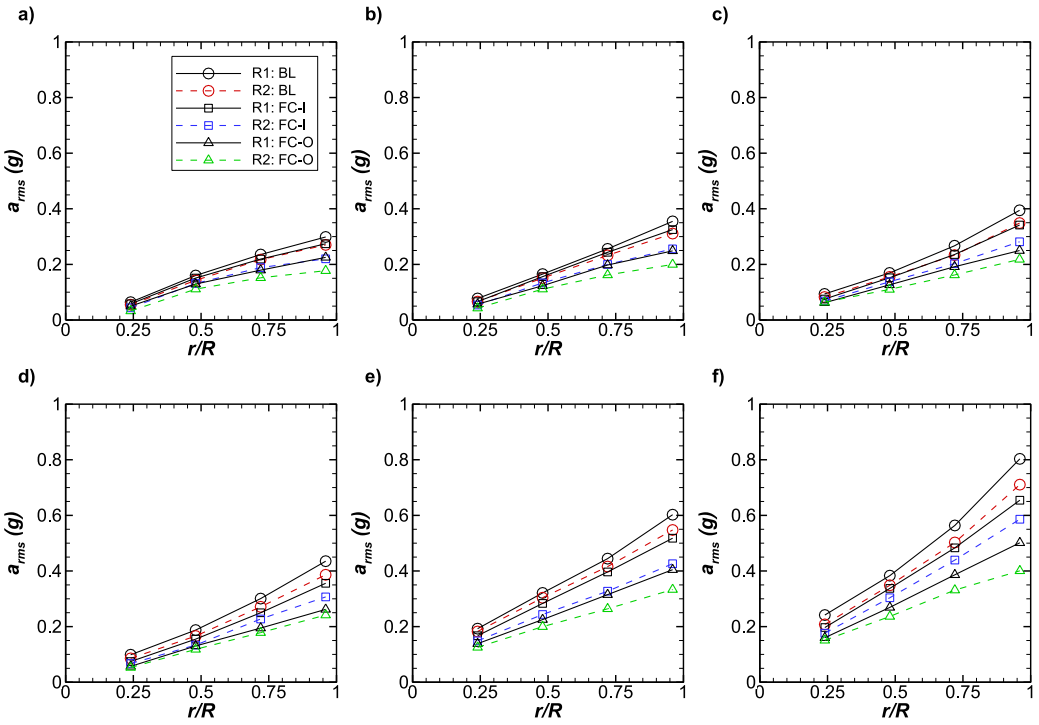

Fig. 10. Root mean square of the blade bending acceleration for R1 and R2 at a rotor speed of $\Omega = 750$ RPM: (a) $\theta_c = 2°$, (b) $\theta_c = 5°$, (c) $\theta_c = 8°$ and $\Omega = 1000$ RPM: (d) $\theta_c = 2°$, (e) $\theta_c = 5°$, (f) $\theta_c = 8°$.

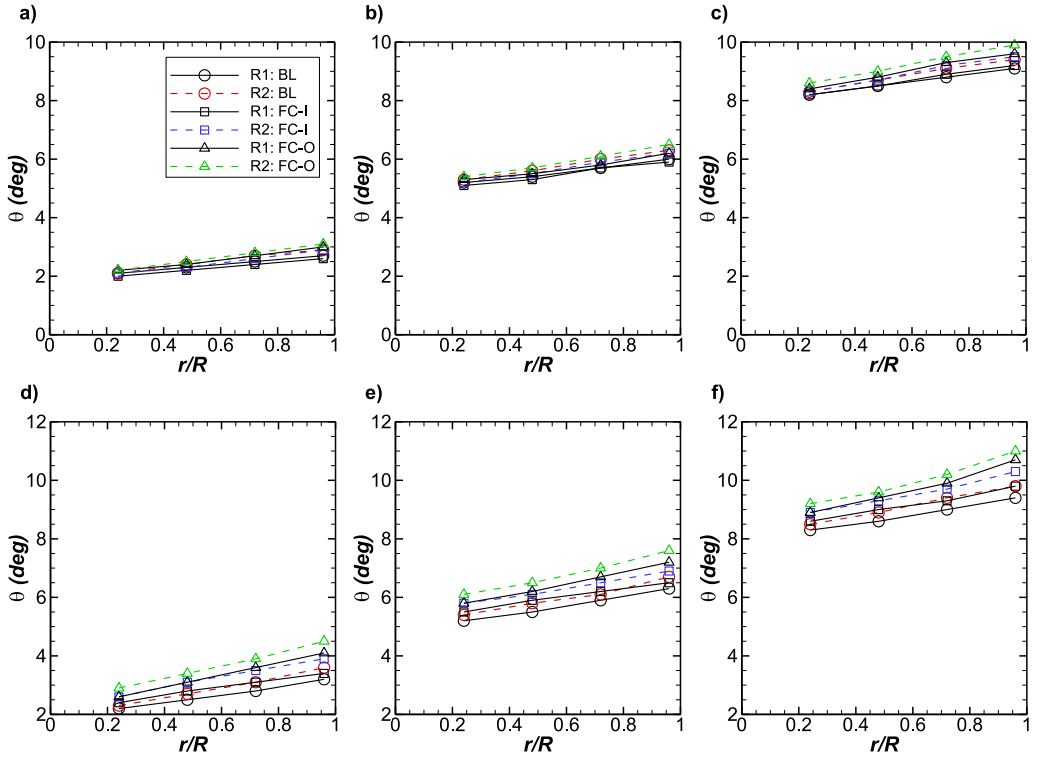

Fig. 11. Mean blade pitch angle for the baseline and flow control cases at a rotor speed of $\Omega = 250$ RPM: (a) $\theta_c = 2°$, (b) $\theta_c = 5°$, (c) $\theta_c = 8°$ and $\Omega = 500$ RPM: (d) $\theta_c = 2°$, (e) $\theta_c = 5°$, (f) $\theta_c = 8°$.

The root mean square of the blade pitch angle, θ_{rms} is presented on Fig. 13 for rotor speeds of $\Omega = 250$ RPM and 500 RPM. The level of θ_{rms} increases along rotor radius, and collective blade pitch angle but remains below $\theta_{rms} = 1.0°$ for all cases. The application of flow control on the inboard of the blade increases θ_{rms} at a rotor speed of 250 RPM due to the effect of synthetic jets with high blowing ratios, $C_b \gtrapprox 3$, which adds a velocity deficit and unsteadiness to the flow that affects the vibration of the blade structure (Maldonado et al., 2021a).

However, for all other rotor speeds especially at $\theta_c = 5°$ and 8°, flow control reduces θ_{rms} by delaying flow separation and reducing the size and strength of a recirculating flow domain

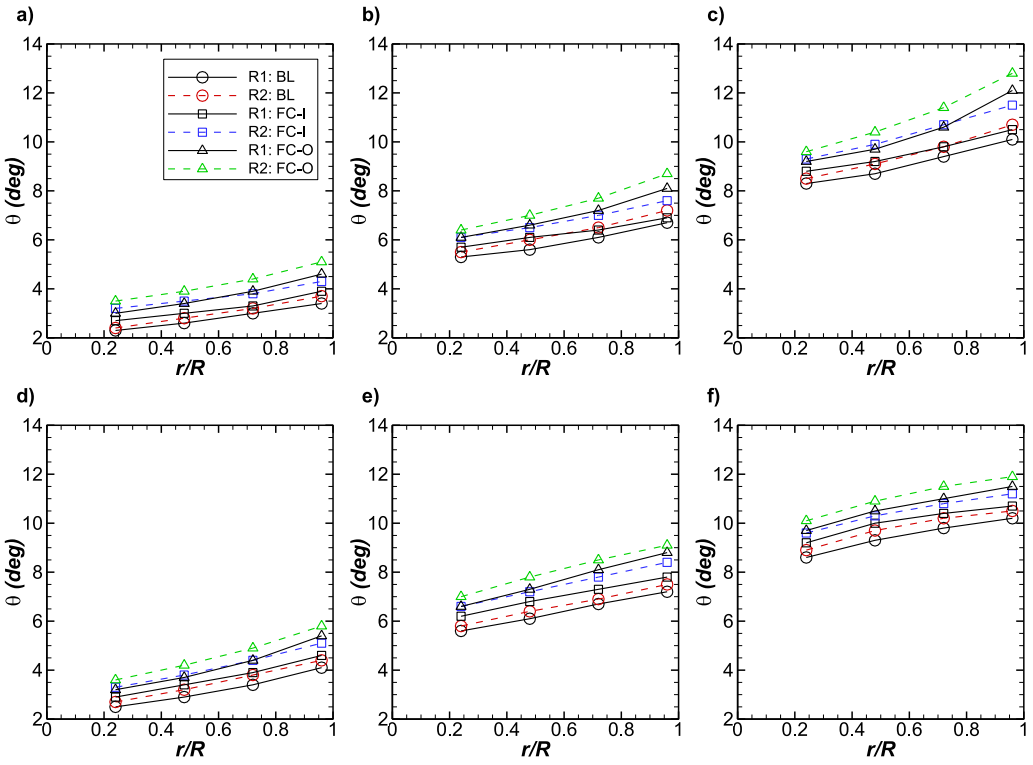

Fig. 12. Mean blade pitch angle for the baseline and flow control cases at a rotor speed of $\Omega = 750$ RPM: (a) $\theta_c = 2°$, (b) $\theta_c = 5°$, (c) $\theta_c = 8°$ and $\Omega = 1000$ RPM: (d) $\theta_c = 2°$, (e) $\theta_c = 5°$, (f) $\theta_c = 8°$.

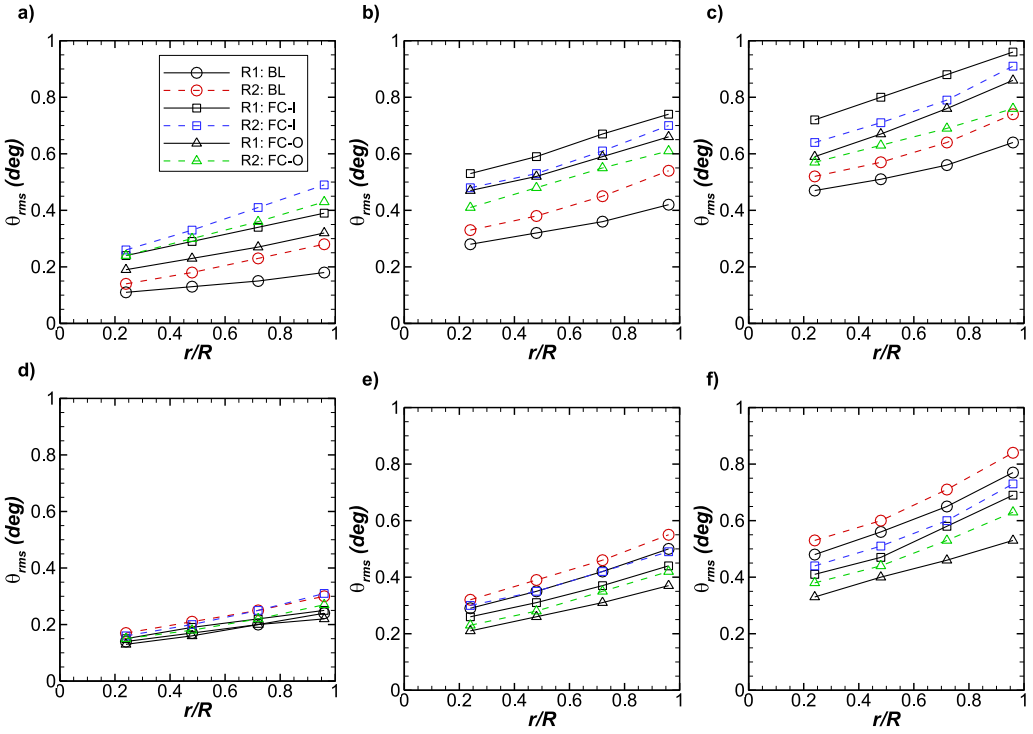

Fig. 13. Root mean square of the blade pitch angle for the baseline and flow control cases at a rotor speed of $\Omega = 250$ RPM: (a) $\theta_c = 2°$, (b) $\theta_c = 5°$, (c) $\theta_c = 8°$ and $\Omega = 500$ RPM: (d) $\theta_c = 2°$, (e) $\theta_c = 5°$, (f) $\theta_c = 8°$.

which appears near the trailing edge of the airfoil and provides unsteady forcing to the structure (Maldonado et al., 2010a). Moreover, activating synthetic jets on the outboard of the blade are more effective than on the inboard in decreasing θ_{rms} because the boundary layers are in an advanced state of transition and instability due to higher Reynolds number, which appears to be where jets are beneficial to the streamwise flow by injecting momentum to the near-wall flow (Maldonado et al., 2021b).

At high rotor speeds, unsteady blade torsion becomes considerably non-linear with rotor radius and the magnitude of θ_{rms}

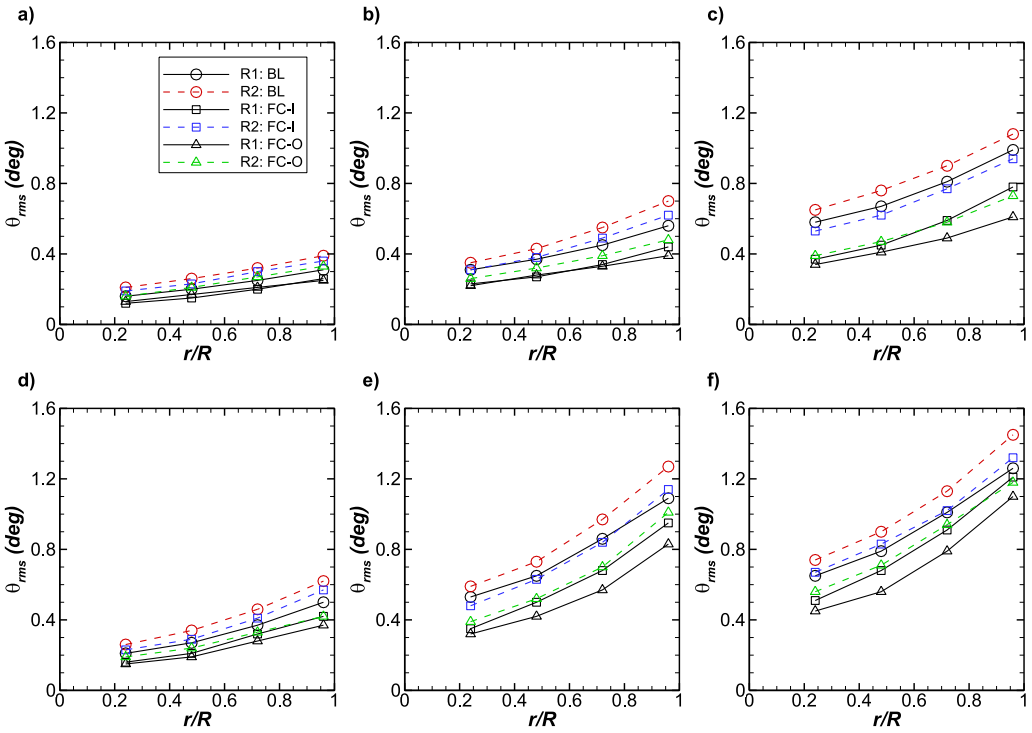

Fig. 14. Root mean square of the blade pitch angle for the baseline and flow control cases at a rotor speed of $\Omega = 750$ RPM: (a) $\theta_c = 2°$, (b) $\theta_c = 5°$, (c) $\theta_c = 8°$ and $\Omega = 1000$ RPM: (d) $\theta_c = 2°$, (e) $\theta_c = 5°$, (f) $\theta_c = 8°$.

increases significantly especially for $\Omega = 1000$ RPM as the collective pitch angle is increased from $\theta_c = 2°$ to 8° in Fig. 14(d) to (f). Rotor 2 baseline reaches a maximum level of unsteady torsion of $\theta_{rms} = 1.45°$ near the blade tip, $r/R = 0.96$ because the flow in this region begins to undergo separation which excites the pitching mode of the blade structure. Flow control applied on the inboard and outboard of the blade decreases θ_{rms} to 1.32° and 1.18° respectively, which represents a decrease of 9% and 22.9% respectively. Alternatively for R1 with a lower blade aspect ratio which is torsionally stiffer, the maximum baseline unsteady torsion at $r/R = 0.96$ is $\theta_{rms} = 1.26°$. Flow control is less effective in reducing θ_{rms} for this blade, representing a decrease of 4% and 12.7% for the inboard and outboard flow control cases.

4. Conclusions

Two rotors with synthetic jets and blade aspect ratio of 7.79 (rotor 1) and 9.74 (rotor 2) representing a difference of 25% were tested to measure key aerodynamics, fluid dynamics, and structural dynamics variables in order to quantify the effect of aspect ratio. It was shown that blade aspect ratio affects flow three-dimensionality, particularly in the mid-region of the blade, and is believed to increases the lift-curve-slope of the blade section and therefore total lift and rotor thrust production. The blade with higher aspect ratio reduces the magnitude of spanwise flow, W/U_∞ by 8%–14% at $r/R = 0.48$, which was correlated to better aerodynamic efficiency via the figure of merit, and is expected to increase the power coefficient of a wind turbine. Flow control did not have a noticeable effect on the spanwise flow, since the synthetic jet velocity is directed along y' which is orthogonal to the spanwise direction z'. However, jets do improve the figure of merit and thrust coefficient particularly at collective pitch angles of 5° and 8°. Perhaps the main finding of this study is that the aerodynamic and aeroelastic performance of the rotor are at odds with each other when increasing blade aspect ratio. While the figure of merit improves with a higher blade aspect ratio, the mean as well as root mean square of blade bending and torsion displacements increase and become more nonlinear. This is undesirable because larger mean and cyclic stresses become transmitted to critical areas of the blade such as the hub, and can reduce the lifetime of these components. While active flow control can be used favorably to reduce the fluctuating component of blade bending and torsion, the mean components and stress is magnified due to the delay of flow separation which increments aerodynamic lift and pitching moment loads.

These results suggest that wind turbine blade engineers must perform a design tradeoff or optimization between aerodynamic efficiency and aeroelastic response depending on the application and atmospheric conditions. For example, wind turbines with higher aspect ratio blades can be installed in zones with lower average wind speeds in order to take advantage of the blade's more efficient aerodynamic characteristics. Active flow control can be selectively applied along the span of the blade, and is generally more effective in the blade tip region, thus eliminating the need for synthetic jets and the additional energy input on the inboard blade region.

Declaration of competing interest

The authors declare that they have no known competing financial interests or personal relationships that could have appeared to influence the work reported in this paper.

Data availability

Data will be made available on request

Funding

This research was supported by the National Science Foundation, USA [Grant No. 1917163].

References

Acar, G.D., Feeny, B.F., 2018. Bend-bend-twist vibrations of a wind turbine blade. Wind Energy 21, 15–28. http://dx.doi.org/10.1002/we.2141.

Akhter, M.Z., Omar, F.K., 2021. Review of flow-control devices for wind-turbine performance enhancement. Energies 14 (5), 1268. http://dx.doi.org/10.3390/en14051268.

Amitay, M., Smith, D.R., Kibens, V., Parekh, D.E., Glezer, A., 2001. Aerodynamic flow control over an unconvenstional airfoil using synthetic jet actuators. AIAA J. 39 (3), http://dx.doi.org/10.2514/2.1323.

Bagai, A., 2008. Aerodynamic design of the X2 technology demonstrator main rotor blade. In: The 64th Annual Forum of the American Helicopter Society. Montreal, Canada.

Cheeseman, I.C., Bennet, W.E., 1955. The Effect of the Ground on a Helicopter Rotor in Forward Flight. ARC R & M, p. 3021.

Gebhardt, C.G., Roccia, B.A., 2014. Non-linear aeroelasticity: An approach to compute the response of three-blade large-scale horizontal-axis wind turbines. Renew. Energy 66, 495–514.

Johnson, S.J., Baker, J.P., van Dam, C.P., Berg, D., 2010. An overview of active load control techniques for wind turbines with an emphasis on microtabs. Wind Energy 13, 239–253.

Kallesoe, B.S., 2011. Effect of steady deflections on the aeroelastic stability of a turbine blade. Wind Energy 14, 209–224.

Kiefer, J., Miller, M.A., Hultmark, M., Hansen, M.O.L., 2016. Effects of finite aspect ratio on wind turbine airfoil measurements. J. Phys. Conf. Ser. 753, 022040. http://dx.doi.org/10.1088/1742-6596/753/2/022040.

Ma, Y., Zhao, Q., Chen, X., Zhao, G., 2020. Experimental analyses of synthetic jet control effects on aerodynamic characteristics of helicopter rotor. Aeronaut. J. 124 (1274), 597–616. http://dx.doi.org/10.1017/aer.2019.163.

Maeda, T., Kamada, Y., Murata, J., Suzuki, D., Kaga, N., Kasigaki, Y., 2014. LDV measurements of boundary layer on rotating blade surface in wind tunnel. J. Phys. Conf. Ser. 555, 012057. http://dx.doi.org/10.1088/1742-6596/555/1/012057.

Maldonado, V., Boucher, M., Ostman, R., Amitay, M., 2010a. Active vibration control of a wind turbine blade using synthetic jets. Int. J. Flow Control 1 (4), 227–238. http://dx.doi.org/10.1260/1756-8250.1.4.227.

Maldonado, V., Farnsworth, J., Gressick, W., Amitay, M., 2010b. Active control of flow separation and structural vibrations of wind turbine blades. Wind Energy 13, 221–237. http://dx.doi.org/10.1002/we.336.

Maldonado, V., Gupta, S., 2019. Increasing the power efficiency of rotors at transitional Reynolds numbers with synthetic jet actuators. Exp. Therm. Fluid Sci. 105, 356–366. http://dx.doi.org/10.1016/j.expthermflusci.2019.04.012.

Maldonado, V., Peralta, N., Ayele, W., Santos, D., 2021a. Aeroelastic response of a propulsive rotor blade with synthetic jets. J. Fluids Struct. 107, 103411. http://dx.doi.org/10.1016/j.jfluidstructs.2021.103411.

Maldonado, V., Peralta, N., Gorumlu, S., Ayele, W., 2021b. On the figure of merit and streamwise flow of a propulsive rotor with synthetic jets. Aerosp. Sci. Technol. 113, 106712. http://dx.doi.org/10.1016/j.ast.2021.106712.

Mittal, R., Rampunggoon, P., 2002. On the virtual aeroshaping effect of synthetic jets. Phys. Fluids 14, 1533.

Ng, B.F., Palacios, R., Kerrigan, E.C., Graham, J.M.R., Hesse, H., 2016. Aerodynamic load control in horizontal wind turbines with combined aeroelastic tailoring and trailing-edge flaps. Wind Energy 19, 243–263. http://dx.doi.org/10.1002/we.356.

Ragni, D., Van Oudheusden, B.W., Scarano, F., 2011. Non-intrusive aerodynamic loads analysis of an aircraft propeller blade. Exp. Fluids 51, 361–371. http://dx.doi.org/10.1007/s00348-011-1057-7.

Rice, T.T., Taylor, K., Amitay, M., 2019. Wind tunnel quantification of dynamic stall on an S817 airfoil and its control using synthetic jet actuators. Wind Energy 22, 21–33.

Taylor, K., Amitay, M., 2015. Dynamic stall process on a finite span model and its control via synthetic jet actuators. Phys. Fluids 27, 077104.

Taylor, K., Leong, C.M., Amitay, M., 2015. Load control on a dynamically pitching finite span wind turbine blade using synthetic jets. Wind Energy 18, 1759–1775. http://dx.doi.org/10.1002/we.1789.

Tibaldi, C., Kim, T., Larsen, T.J., Rasmussen, F., de Rocca Serra, R., Sanz, F., 2016. An investigation on wind turbine resonant vibrations. Wind Energy 19, 847–859. http://dx.doi.org/10.1002/we.1869.

Velasco, D., Lopez Mejia, O., Lain, S., 2017. Numerical simulations of active flow control with synthetic jets in a Darrieus turbine. Renew. Energy 113, 129–140. http://dx.doi.org/10.1016/j.renene.2017.05.075.

Yen, J., Ahmed, N.A., 2013. Enhancing vertical axis wind turbine by dynamic stall control using synthetic jets. J. Wind Eng. Ind. Aerodyn. 114, 12–17. http://dx.doi.org/10.1016/j.jweia.2012.12.015.

Zhang, M., Tan, B., Xu, J., 2015. Parameter study of sizing and placement of deformable trailing edge flap on blade fatigue load reduction. Renew. Energy 77, 217–226. http://dx.doi.org/10.1016/j.renene.2014.12.022.